

40 Gb/s Field-Modulated Wavelength Converters for All-Optical Packet Switching

Matthew M. Dummer, *Student Member, IEEE*, Jonathan Klamkin, *Student Member, IEEE*,
Anna Tauke-Pedretti, *Member, IEEE*, and Larry A. Coldren, *Fellow, IEEE*

(Invited Paper)

Abstract—We present a high-functionality photonic integrated circuit that performs field-modulated wavelength conversion. This device incorporates an on-chip sampled grating distributed Bragg reflector laser for wide tunability. Wavelength conversion is accomplished using a preamplified semiconductor optical amplifier photodiode receiver interconnected with a traveling-wave modulator to form a high-speed optical gate. This paper discusses the design and performance of this device, as well as its potential for optical packet switching applications. Error-free wavelength conversion is demonstrated at 40 Gb/s with 1–3 dB power penalty compared with back-to-back transmission over 22 nm of input and output tuning. Output extinction in all cases is greater than 9 dB, and conversion efficiency ranges from –2 to –6 dB over the tuning range. This device additionally demonstrates the capability for external 10 Gb/s modulation, which can be used for optical label encoding.

Index Terms—Electroabsorption, semiconductor amplifiers, traveling-wave devices, tunable lasers, undercut etching, wavelength conversion.

I. INTRODUCTION

THE WIDESPREAD use of wavelength-division multiplexing (WDM) has greatly increased the capacity in today's fiber optic networks. As WDM networks continue to grow in complexity, methods for dynamic wavelength management, and especially wavelength conversion, have become increasingly important. Wavelength conversion allows for effective resolution of signal contention in high traffic networks, allowing for better utilization of available network bandwidth [1]. Furthermore, wavelength converters have been proposed as the key switching elements for all-optical routing in next-generation networks.

The capacity of today's optical–electronic–optical (OEO) routing architecture is rapidly approaching its limit in terms of processing and buffering requirements, as well as overall power dissipation. To resolve these issues, future networks will necessitate that many of the routing functions be performed in the optical domain. One solution that has been offered is all-optical label switching, which allows individual IP packets to

be optically routed by dynamic wavelength assignment [2]. In this type of routing architecture, individual labels that accompany each payload are identified by the node, and the destination of the packet is determined using a lookup table. The output of a wavelength converter is then tuned to the proper wavelength to route the packet through an arrayed waveguide grating to the desired port. This type of architecture allows for minimal electronic processing and can support very high bit rates, since only the labels must be electronically recovered at each node.

Making the leap to optically packet switched networks will require an efficient and scalable technology for performing high-speed wavelength conversion. Photonic integrated circuits (PICs) are an attractive solution for achieving high functionality with low cost. Compared with discrete optical components, such as PICs offer small footprint, simplified packaging, low optical loss, and reduced power dissipation, all of which are necessary for a viable wavelength conversion technology.

Of particular interest are PICs that incorporate a widely tunable laser source on chip. To date, two different methods for single-chip wavelength conversion have been demonstrated. The first of these is a carrier-modulated approach, which takes advantage of nonlinearity in a semiconductor optical amplifier (SOA) to achieve cross-gain modulation (XGM) or cross-phase modulation (XPM) between an input data signal and the on-chip continuous-wave (CW) signal [3]. The switching speed of these devices is limited by the carrier lifetime in the saturated SOA, which typically limits the operating bandwidth to 10 Gb/s. However, more recently, differential interference techniques have been used to demonstrate 40 Gb/s in a monolithic device [4], [5].

An alternative approach to wavelength conversion is based on modulation of the electric field, as opposed to modulation of the carrier density in the SOA case. Field-modulated devices make use of an interconnected photodiode (PD) and either an electroabsorption modulator (EAM) or Mach–Zehnder modulator (MZM) to form a high-speed optical gate. Such optical gates have been used to demonstrate wavelength conversion at data rates as high as 100 Gb/s [6]. The field-modulated approach offers a number of advantages for optical routing applications. These include increased network transparency, conversion to a similar (or the same) wavelength as the input signal, and elimination of optical filtering requirements at the output. Furthermore, field-modulated wavelength converters have demonstrated the potential for 2R, or 3R regeneration [7], which will be beneficial for cascaded optical routing through multiple nodes.

Manuscript received November 1, 2008; revised February 10, 2009. First published May 8, 2009; current version published June 5, 2009. This work was supported by the Defense Advanced Research Projects Agency (DARPA) MTO-LASOR under Grant W911NF-04-9-0001.

The authors are with the Department of Electrical and Computer Engineering and the Department of Materials, University of California Santa Barbara, Santa Barbara, CA 93106 USA (e-mail: dummer@engineering.ucsb.edu).

Color versions of one or more of the figures in this paper are available online at <http://ieeexplore.ieee.org>.

Digital Object Identifier 10.1109/JSTQE.2009.2017279

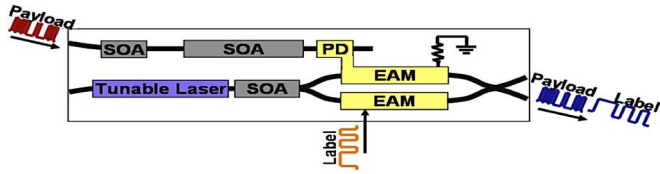


Fig. 1. Schematic diagram of the device design depicting both wavelength conversion and label writing functionalities.

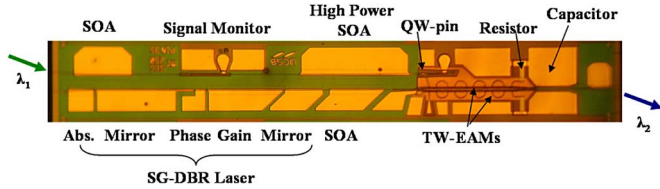


Fig. 2. Photograph of fabricated wavelength converter. The total footprint is $4.1 \text{ mm} \times 0.55 \text{ mm}$.

In previous monolithic devices, 10 Gb/s operation has been demonstrated using an EAM [8], and 40 Gb/s operation has been demonstrated with a series push-pull MZM [9]. This paper presents the first demonstration of monolithic 40 Gb/s wavelength conversion using an electroabsorption-based device. Error-free operation with less than 3 dB power penalty is achieved over 22 nm of input and output tuning range.

For efficient utilization of bandwidth in optical packet switching, it is desirable for the optical label to be encoded on the same carrier wavelength as its corresponding payload. Therefore, we have designed this device with the capability to encode 10 Gb/s labels as well, using a separate modulation region. Over the same wavelength range, 10 Gb/s transmission is demonstrated error-free.

II. DEVICE ARCHITECTURE AND FUNCTIONALITY

This wavelength converter incorporates all of the elements of a widely tunable transceiver onto a single InP chip. The device is comprised of two separate waveguide regions that are responsible for the receiver and transmitter functionality. A schematic depicting the general layout of the wavelength converter is shown in Fig. 1. On the receiver side, there are two SOA preamplifiers followed by a high-power p-i-n PD. The transmitter side contains a widely tunable sampled grating distributed Bragg reflector (SG-DBR) laser, consisting of a gain and phase section between two SG mirrors, followed by an output SOA. The light from the SG-DBR laser is divided into two parallel traveling-wave EAMs using a 1×2 multimode interference (MMI) splitter. One of the EAMs is directly connected to the PD to form a high-speed optical gate to perform wavelength conversion. The other EAM can be electrically driven to function as a transmitter for encoding labels onto individual IP payloads. The two EAM branches are combined again by a 2×2 MMI before being emitted from the chip. The parallel EAM configuration allows the wavelength conversion and label-writing functions to take place independent of one another, with a simple bias configuration. A picture of the final fabricated device is shown in Fig. 2.

The operation of the optical gate for wavelength conversion can be described by a three-step process, as shown in Fig. 3.

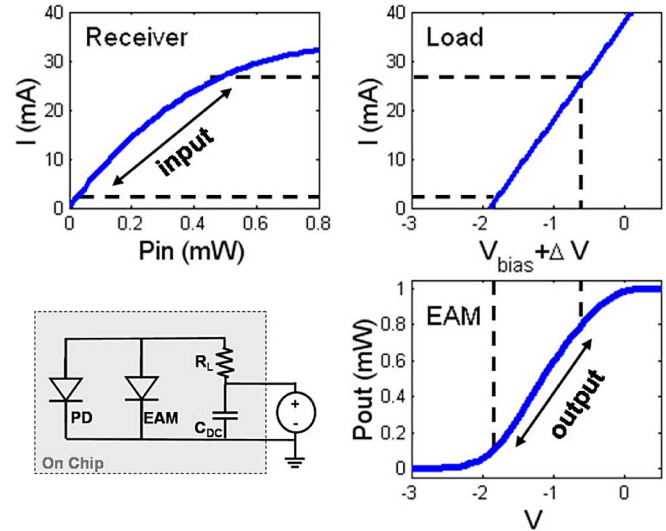


Fig. 3. Example of the three-part transfer function for the field-modulated optical gate. Circuit diagram is shown in the lower left.

First, the input signal, which is optically preamplified by the receiver SOAs, is incident on the PD to generate photocurrent. This current is dissipated by a load resistor, which provides the transimpedance to change the voltage across the EAM. The corresponding change in electric field reduces the absorption in the EAM from its normally “OFF” state, thereby opening the gate. In this way, the input signal can be transcribed onto any new output wavelength within the tuning range of the SG-DBR. The efficiency of the gate is dependent on the gain of the receiver and the extinction characteristics of the EAM, as well as the resistor value selection. The individual component performance will be further discussed in Section IV.

For this device, a thin-film load resistor has been integrated onto the chip. A dc-blocking capacitor is also incorporated to allow for simple reverse biasing of the PD and EAM with a single dc voltage. The on-chip termination allows wavelength conversion to be performed without any external microwave circuitry or bias tees, and greatly simplifies packaging and operation [8]. The bias configuration is shown in Fig. 3. A similar resistor and capacitor are also used to terminate the label-writing EAM.

III. DUAL QUANTUM WELL INTEGRATION PLATFORM

As described before, this field-modulated wavelength converter requires the integration of four types of optical components with diverse functionalities. These include the gain elements, i.e., laser and amplifier, and the absorption elements, i.e., modulator and PD. In addition, low-loss passive regions are also desirable for transporting signals between the components. Therefore, a versatile integration platform is essential for achieving optimal device performance. In this case, we have adopted a dual quantum well (DQW) integration platform as described in [10].

The epitaxial layer structure consists of a single InGaAsP waveguide core surrounded by upper and lower InP cladding layers shown in Fig. 4. Within the core, there are two different multiquantum well stacks. An upper set of seven offset quantum

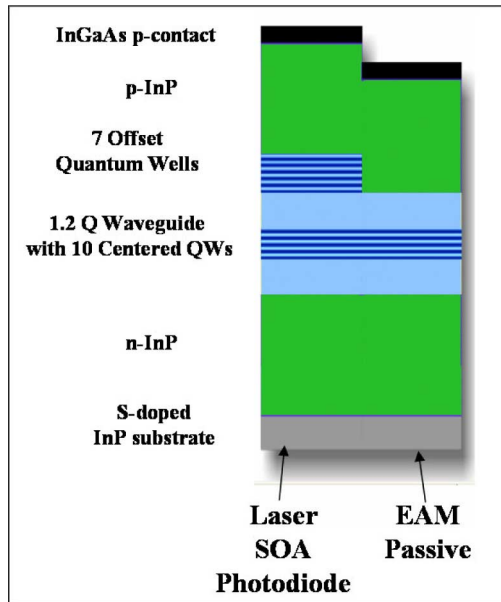


Fig. 4. DQW integration platform. The layer structure chosen for each region of the chip is denoted.

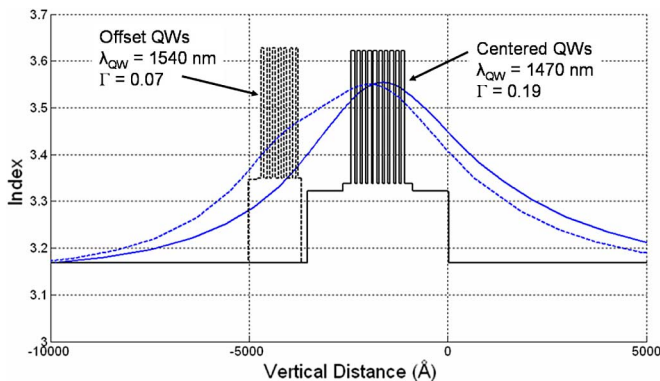


Fig. 5. Index and optical mode profile for the “active” (dotted) and “passive” (solid) regions of the device.

wells (OQWs) with a band edge corresponding to 1540 nm is used to provide optical gain. A second set of ten quantum wells centered in the core (CQW) is detuned 70 nm from the operating wavelength ($\lambda_{QW} = 1470$ nm) and is used to provide modulation efficiency under reverse bias. Active and passive regions of the device are defined by selectively removing the OQWs prior to regrowth of the upper InP cladding. A simulation of the optical mode profile in both the active and passive sections is shown in Fig. 5.

The DQW platform is advantageous because it can be implemented with only a single blanket regrowth, and therefore, allows for relatively simple fabrication and high yield. However, because this platform provides only two distinct bandgap regions within the chip, there are inherent tradeoffs in performance for each of the device components. For example, because both the SOAs and the laser make use of the same OQW gain material, a compromise must be made between the laser gain and amplifier saturation power. Similarly, because the CQWs

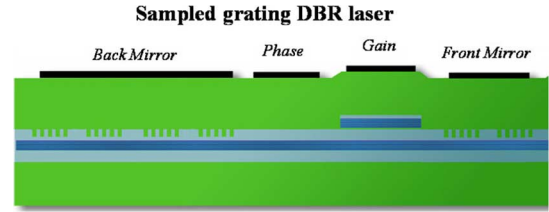


Fig. 6. Schematic of the SG-DBR laser cross section showing the waveguide structure of the gain, phase, and mirror sections.

are present throughout the entire wafer, the band edge of these wells must be carefully chosen to balance modulation efficiency of the EAM under reverse bias with passive waveguide loss in the unbiased regions. Finally, the DQW does not allow for an optimal PD structure to achieve both high bandwidth and high saturation power. While the best reported high-power PDs typically make use of bulk absorbing in conjunction with an intricate doping scheme, as in untraveling carrier (UTC) [11], [12] or partially depleted absorbers (PDAs) [13], this is not possible without an additional regrowth. For simplicity, we have instead chosen to implement a QW pin detector by using the offset gain region under reverse bias as the absorbing medium. By proper design of the device geometry, these PDs are capable of high-bandwidth operation (40 Gb/s) and good responsivity (1.00 A/W).

IV. INTEGRATED COMPONENTS AND CHARACTERIZATION

The performance of each of the integrated components has been optimized within the limits of the DQW platform. Here, we discuss the design and the characterization of these components, and their overall impact on the performance of the wavelength converter.

A. SG-DBR Laser

The SG-DBR laser was chosen for this paper because of its robust fabrication process and ease of integration. The laser consists of a 550- μm -long active gain section and a 50- μm -long phase section, surrounded by two mirrors, as shown in Fig. 6. The mirrors make use of periodic gratings, patterned by holographic lithography, to obtain a comb-like reflectivity spectrum. Because the sampling period differs between the front and back mirrors, current injection can be used to shift the relative reflectivity of each of the mirrors to select out a single supermode. This principle allows for Vernier-based tuning to achieve lasing over a wide wavelength range [14].

Fig. 7 shows the measured *LIV* characteristic for the integrated laser. The optical power was measured on chip by reverse biasing the output SOA. The threshold current for the device is 45 mA, and 19 mW of power is possible when biased up to 150 mA. The 400- μm -long output SOA additionally produces up to 6 dB of gain. However, it is typically driven with a lower current to limit the amplified spontaneous emission (ASE) contribution. The laser demonstrates continuous tuning over the range of 1524–1564 nm, as shown by the overlaid supermode spectra in Fig. 8. The fiber-coupled output power after the modulation

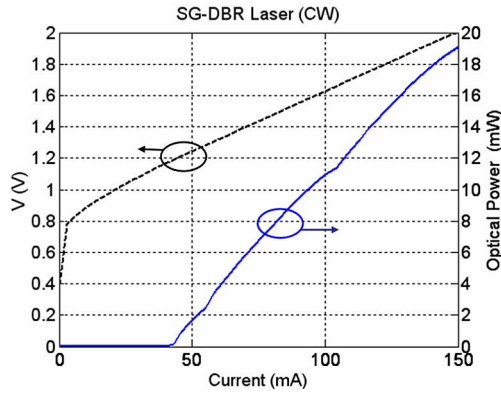
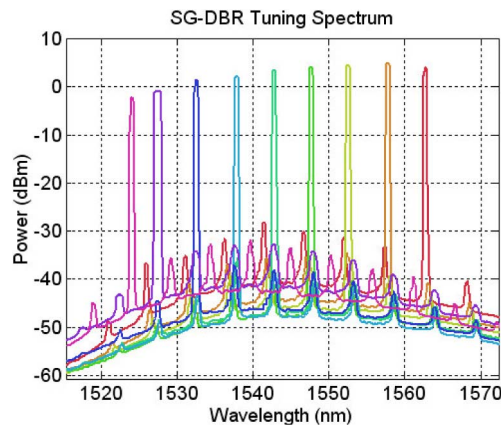
Fig. 7. SG-DBR laser *LIV* characteristic.

Fig. 8. Overlaid output spectra of nine supermodes from the SG-DBR laser.

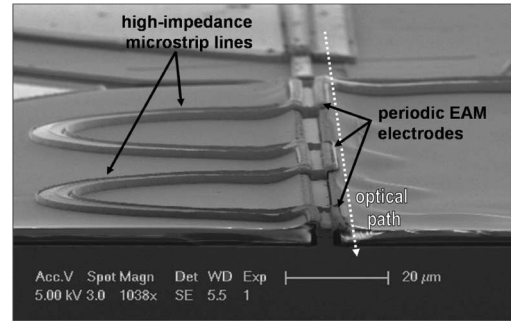
region ranges from -2 to 4 dBm, and greater than 30 dB side-mode suppression is observed over the entire tuning range.

B. Traveling-Wave EAMs

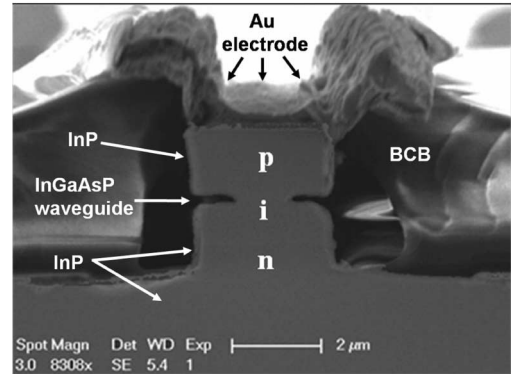
For the modulators in this paper, we have implemented a traveling-wave (TW) electrode design such that the electrical signal copropagates with the optical wave to achieve coherent interaction along the device length. With this configuration, it is possible to surpass the traditional RC frequency limitation of the device so that very high bandwidth can be achieved. In a TW-EAM, the instantaneous forward traveling voltage on the electrode is directly proportional to the characteristic impedance Z_0

$$V^+ = Z_0 I_{\text{photo}}. \quad (1)$$

Therefore, for the given amount of photocurrent from the PD (I_{photo}), it is advantageous to raise Z_0 to achieve a higher drive voltage, and consequently, improve the modulation efficiency. Here, we have implemented two techniques for raising the characteristic impedance, both of which involve reducing the capacitance per length of the TW-EAM. The first is selective undercut etching of the modulator waveguide to reduce the underlying junction capacitance [15], [16]. This requires first transitioning from a surface ridge waveguide into a deeply etched structure in



(a)



(b)

Fig. 9. SEMs of a high-impedance TW-EAM structure. (a) Periodic microstrip electrode design. The modulator has been cleaved halfway along the length. (b) Cross section of the ridge waveguide with selectively undercut intrinsic region for low capacitance.

the modulator region. A lateral selective wet etch with sulphuric acid and hydrogen peroxide is then used to reduce the width of the InGaAsP intrinsic region. In this case, the EAM waveguide width has been reduced from $3 \mu\text{m}$ down to $1.1 \mu\text{m}$ wide, as shown in the SEM cross section in Fig. 9.

The second technique that has been utilized is periodic loading of the transmission-line structure. By alternating between high-impedance microstrip sections and capacitively loaded modulation sections, a higher average impedance can be achieved [17]. The EAMs in this paper are designed with five $50 \mu\text{m}$ stages for a total modulation length of $250 \mu\text{m}$. The periodic electrode, as shown in Fig. 9, uses a 1:3 ratio of loaded to unloaded sections. The lengths of the electrical and optical paths through the EAM are designed such that the propagation times are equal to provide effective velocity matching. Together with the undercut etched waveguide, the periodic electrode structure effectively doubles the characteristic impedance of the TW-EAM from 20 to 40Ω . The integrated load resistor value (25Ω) is intentionally lower than Z_0 to create a resonant reflection that leads to an enhancement in the frequency response. From previously fabricated modulator test structures, we estimate the 3-dB bandwidth of the TW-EAM to be >45 GHz.

The dc extinction of the TW-EAM has been measured across the tuning range of the SG-DBR laser. Fig. 10 shows the extinction characteristics for varying reverse bias. The peak modulation efficiency ranges from 10 to 14 dB/V over 30 nm of

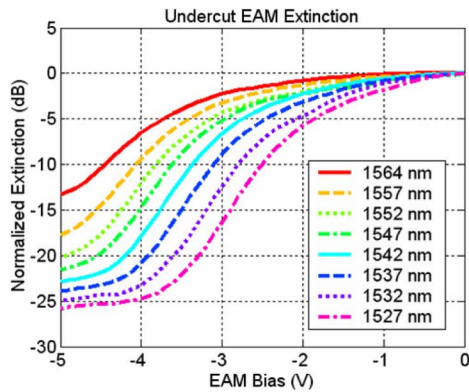


Fig. 10. DC extinction characteristic for the 250- μm TW-EAM over the tuning range of the SG-DBR.

wavelength tuning. The efficiency is the highest at the shortest wavelength, where the detuning from the absorption edge of the CQW is the least. However, the shorter wavelengths also incur higher insertion loss. The modal passive waveguide loss in the device has been measured to be between 4 and 11 cm^{-1} (1.74–4.78 dB/mm) for wavelengths from 1562 to 1528 nm. The undercut waveguide structure in the EAM adds an additional 7 cm^{-1} (3.0 dB/mm) of modal loss. This is possibly due to increased overlap of the mode with the zinc-doped upper InP cladding in this region, which results in higher absorption.

C. SOA-PD Receiver

Since there is no electronic amplification of signals in this device, wavelength conversion relies on directly driving the EAM with the photocurrent from the PD. Therefore, achieving high saturation power in the SOAs and PD is very important for generating high voltage swing and minimal pattern dependence caused by slow carrier lifetimes. The two-section receiver SOA uses a short (400 μm) gain stage followed by a long (800 μm) high-power stage. The two-stage design enables independent biasing of the two amplifiers so that the input power into the second stage can be adjusted to achieve the maximum output without signal degradation. A signal monitor pad between the two SOAs offers the possibility for implementing automatic gain control with an external feedback circuit, although this has not yet been demonstrated.

The low confinement factor (0.07) of the OQW gain region is beneficial for providing SOAs with high saturation power. To further increase the saturation power in the second stage, the width of the waveguide is flared to reduce the optical power density as the total power increases. By linearly flaring the the ridge from 3 to 12 μm wide, the saturation power can be increased by 4 dB [18]. In this case, the 1-dB output compression power of the second receiver SOA is 16.3 dBm.

Under reverse bias, the OQW material provides a modal absorption coefficient of 450 cm^{-1} , which allows for short PDs with high quantum efficiency. However, using QWs as the absorbing medium in the PD introduces the possibility of space charge accumulation under high-power illumination. To improve the saturation power of the QW-PD, the front end of

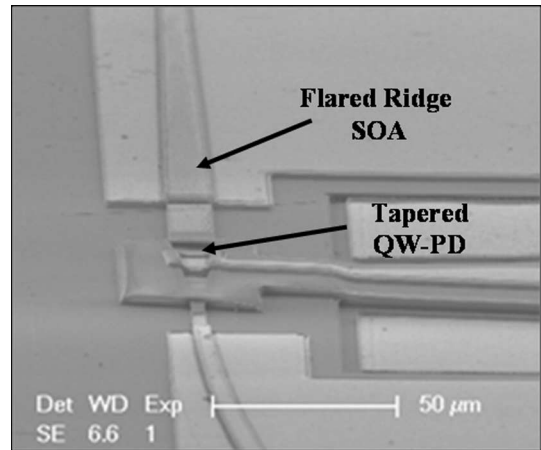


Fig. 11. SEM of the receiver depicting the flared ridge SOA followed by the high-power QW PD.

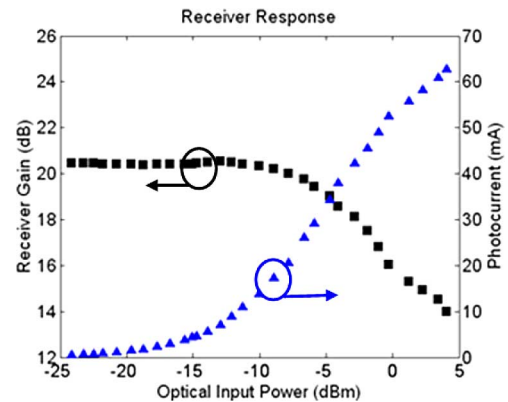


Fig. 12. Measured receiver gain and generated photocurrent as a function of input power.

the detector is kept wide, similar to the SOA, to reduce the optical power density. As the power is absorbed along the length, the waveguide is tapered to reduce the total capacitance. An SEM of the receiver structure depicting the flared and tapered waveguide is shown in Fig. 11. For the 35- μm -long PD, tapered from 9 to 5 μm , the bandwidth is greater than 20 GHz and -3 V bias is sufficient to maintain unsaturated operation with 20 mA of average photocurrent.

Because the gain material is comprised of compressively strained QWs, the receiver is highly polarization sensitive. Therefore, the input polarization was adjusted to TE orientation in all experiments. Fig. 12 shows the gain and photocurrent generated by the receiver for a 1550-nm CW input signal. For dc biases of 70 and 310 mA on the two SOAs and -3.0 V on the QW pin PD, the total gain of the receiver is about 20 dB. The maximum photocurrent observed is greater than 60 mA. However, at this operating point, the SOA gain has significantly rolled off due to saturation. The 1-dB gain compression point occurs at an input power of -6 dBm. This corresponds to 32 mA of linear dc photocurrent available for driving the TW-EAM.

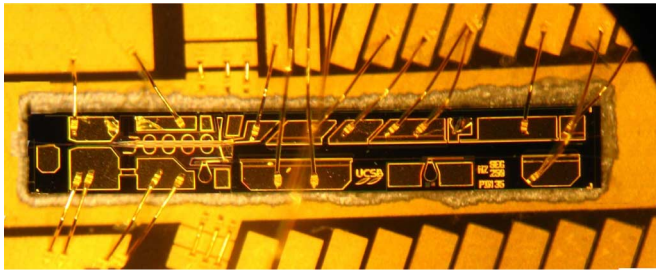


Fig. 13. Photograph of DUT mounted and wirebonded to an AlN carrier.

V. WAVELENGTH CONVERSION EXPERIMENTS

A series of wavelength conversion experiments have been performed to characterize the overall device performance. For these experiments, the device was soldered to an aluminum nitride carrier and wirebonded such that a single dc probe card could be used to apply all dc biases (Fig. 13). A $0.22\text{-}\mu\text{F}$ capacitor was mounted on the carrier and placed in parallel with the on-chip capacitor to improve the low-frequency response of the optical gate circuit. Input and output signals were coupled to and from the chip using conically tipped lensed fibers. The temperature of the copper test stage was maintained at 13°C during these experiments to achieve the optimal gain in the SOAs.

A. Small-Signal Response

Although this device was designed for large-signal digital modulation, small-signal measurements are useful for characterizing the microwave circuit design and observing the carrier dynamics within the receiver. Fig. 14 shows the normalized optical-to-optical small-signal response for conversion from 1548 to 1554 nm. The transmitter and receiver were biased such that the average photocurrents in the EAM and PD were 8.5 and 20 mA, respectively. Over the measurement range, a broadband inductive peak is observed due to the high-impedance electrode design in the EAM. For reverse biases greater than 3 V, there is no degradation in the response up to 20 GHz. For less than 3 V reverse bias, the corresponding applied field in the PD is insufficient to quickly sweep the generated carriers out of the junction. The accumulation of localized space charge can be recognized by the resulting degradation in the device bandwidth. The small resonance in the response at 1 GHz is caused by the inductance of the wirebond used to bias the optical gate [8].

B. Digital Performance

The wide bandwidth of this device makes it well suited for high-speed digital operation. To characterize the large signal behavior, we have examined the bit error rate (BER) performance using pseudorandom bit sequences (PRBSs) at 40 Gb/s with nonreturn-to-zero (NRZ) format. The experimental setup used for these digital wavelength conversion measurements is shown in Fig. 15. PRBS data generated by a BER tester (BERT) was used to modulate an optical transmitter, and was passed through an erbium-doped fibre amplifier (EDFA), optical filter, polarization controller, and attenuator, before being coupled into the device under test (DUT). The converted output signal

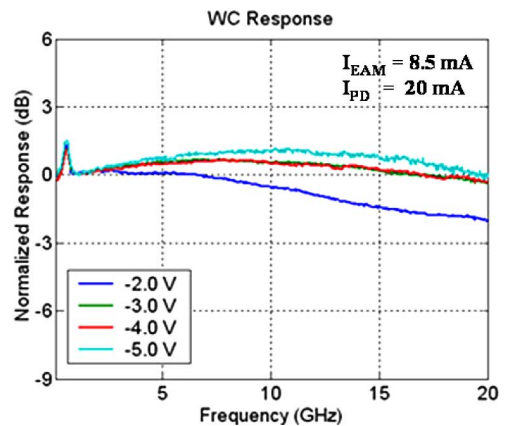


Fig. 14. Small-signal optical-to-optical response of the wavelength converter.

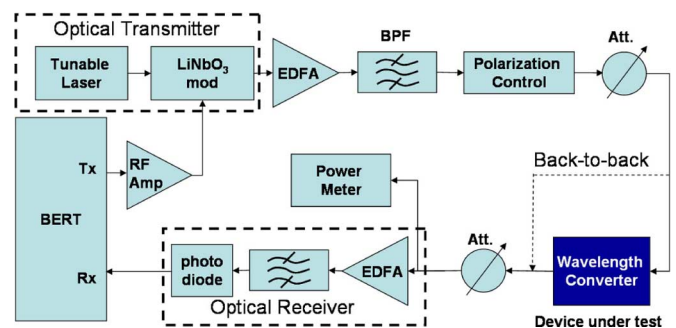


Fig. 15. Measurement setup for characterization of the wavelength conversion performance. BER of converted signal is compared to back-to-back transmission for varying power into the optical receiver.

was passed through a second attenuator, followed by an optically preamplified receiver that was connected back to the error analyzer of the BERT. The attenuator following the DUT was used to reduce the power into the receiver to a level at which errors could be recorded. The resulting BER for each received power was then compared with back-to-back transmission to compute a power penalty. The word length in these experiments was limited to $2^7 - 1$ because of pattern-dependent effects in the measurement setup.

Before measuring the BER over the wavelength tuning range, the optimal input power and operating conditions for the device were determined. The optimal bias point for the receiver SOAs was found to be 9 kA/cm^2 , which corresponded to the highest gain and saturation power. The laser gain section and the transmitter SOA were biased with lower current density (5.8 and 2.5 kA/cm^2 , respectively) to limit the EAM photocurrent and reduce thermal crosstalk. The bias of the optical gate was chosen to take advantage of the highest modulation slope efficiency for the output wavelength of the SG-DBR. Using these conditions, the input power into the device was varied to determine the best BER, as shown in Fig. 16(a), for wavelength conversion from 1550 to 1548 nm. From this measurement, we have extracted the power penalty measured at a BER of 10^{-9} between back-to-back and the wavelength-converted signals, as shown in Fig. 16(b). Also measured were the extinction ratio of the output signal and the wavelength conversion efficiency, defined

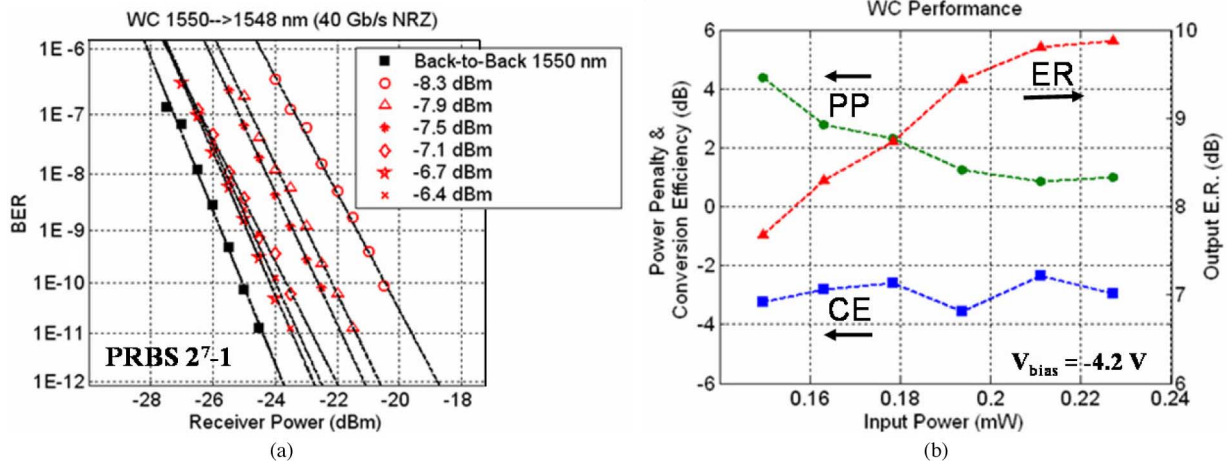


Fig. 16. (a) 40 Gb/s BER measurements for wavelength conversion from 1550 to 1548 nm for varying optical input power compared with back-to-back transmission. (b) Measured power penalty (PP) at BER of 10^{-9} , output extinction ratio (ER), and facet-to-facet conversion efficiency (CE) at each input power.

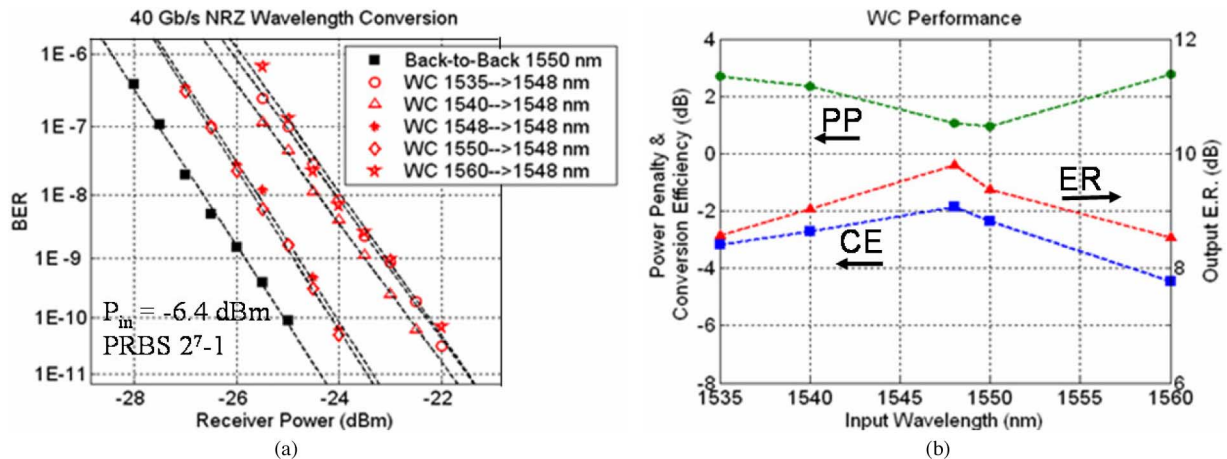


Fig. 17. (a) 40 Gb/s BER measurements for varying input wavelength and constant output wavelength for input power of -6.4 dBm. (b) Measured power penalty (PP), output extinction ratio (ER), and conversion efficiency (CE) versus input wavelength.

as the ratio of power between the converted signal and the input signal at each facet. Since no mode converters were present in this design, the fiber coupling loss added an additional 4 dB of loss at each facet.

The dynamic range measurements show that the output extinction ratio increases with input power, resulting in a reduction in the power penalty. As the input power approaches the 1-dB saturation point of the receiver SOA, the output extinction begins to level off due to the reduced gain. Input powers above -6.4 dBm were not tested with these bias conditions to avoid damaging the PD, since failure has been observed at 200 mW of dissipated power. Operation with input powers as high as $+5$ dBm was possible by adjusting the bias of the first SOA stage to reduce the total gain. This, however, resulted in significant reduction in conversion efficiency.

Wavelength conversion performance was evaluated as a function of input wavelength. Fig. 17(a) shows the resulting BER measurements for varying input wavelength with -6.4 dBm input power. Error-free wavelength conversion was observed over the range of 1535–1560 nm. The measured power penalty,

extinction, and conversion efficiency are shown in Fig. 17(b). Less than 3 dB power penalty is observed over the tuning range compared with back-to-back transmission. This includes the case of conversion back to the same wavelength (1548 nm to 1548 nm). The device exhibits the best performance when the input wavelength corresponds to the gain peak of the receiver. This results in a power penalty of 1 dB and a conversion efficiency of -2 dB.

BER measurements of wavelength conversion to varying output wavelengths have also been performed. Fig. 18 shows the BER measurements for three output wavelengths: 1537, 1548, and 1559 nm. For these measurements, the back-to-back data were compared at the same wavelength as the output from the device to eliminate the wavelength dependence in the measurement setup. The bias of the optical gate was adjusted to achieve the lowest power penalty at each wavelength. Error-free transmission was observed in all three cases with less than 1 dB power penalty. Fig. 19 shows the converted 40 Gb/s eye diagrams, which were taken at the lowest power penalty for each wavelength. The output extinction and bias condition are listed

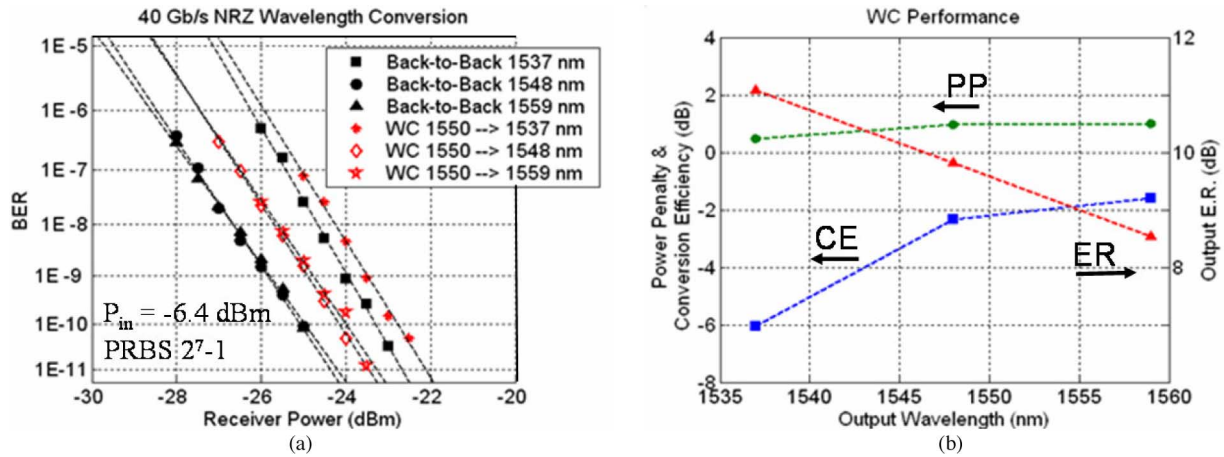


Fig. 18. (a) 40 Gb/s BER measurements for fixed input wavelength and varying output wavelength for input power of -6.4 dBm. (b) Measured power penalty (PP), output extinction ratio (ER), and conversion efficiency (CE) versus output wavelength.

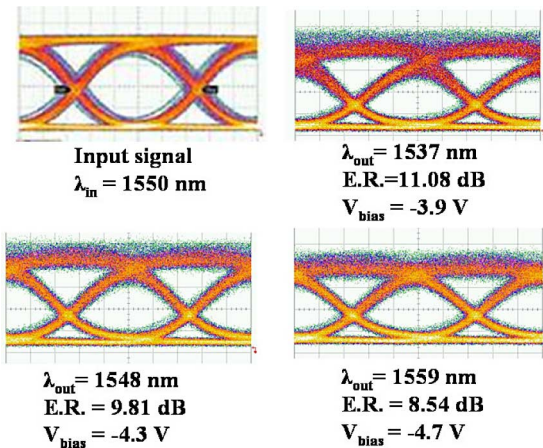


Fig. 19. 40 Gb/s NRZ input and wavelength-converted eye diagrams corresponding to the BER measurements in Fig. 18. Gate bias and output extinction are listed.

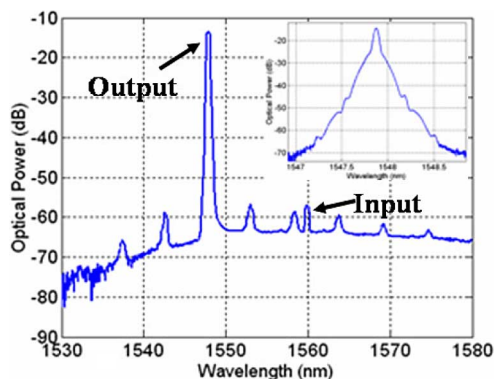


Fig. 20. Output optical spectrum from the wavelength converter demonstrating 45 dB input suppression. Inset shows higher resolution plot of the output signal with 40 Gb/s modulated data spectrum.

for each case. The summary of performance in Fig. 18(b) exemplifies the tradeoff introduced by the wavelength dependence of the EAM. For shorter wavelengths, the modulation efficiency is higher, which produces greater extinction. However, the passive optical loss is also increased, which leads to lower output power,

TABLE I
OPERATING CONDITIONS AND TOTAL POWER DISSIPATION

	V (V)	I (mA)	P (mW)
SG-DBR Gain	1.7	115	195.5
Trans. SOA	1.6	60	96
Rec. SOA 1	2.1	100	210
Rec. SOA 2	2.1	300	630
Mirrors / Phase	1.3	50	65
PD	-4.2	28	117.6
EAM 1	-4.2	12	50.4
EAM 2	-4.2	12	50.4
Load Resistor	1	40	40
Total			1454.9

and hence lower conversion efficiency. The opposite result occurs for the longer output wavelength; however, in all cases, the total power penalty remains relatively constant.

The optical spectrum of the converted output signal is shown in Fig. 20 for input and output wavelengths of 1560 and 1548 nm, respectively. Because of the spatial separation of the input and output signals within the device, the input suppression ratio at the output is greater than 40 dB. As shown in Fig. 20, the input power level is on the same order as the side-mode suppression of the SG-DBR laser.

The total power dissipation of the device has also been calculated. The normal operating conditions and the power contribution from each component on the chip are listed in Table I. During wavelength conversion of PRBS data, the total power dissipation is slightly lower than 1.5 W. For no input signal, or for bursts of data with short duty cycles, the power dissipation is reduced to around 1.35 W due to lower average photocurrent generated in the optical gate.

VI. LABEL WRITING

The capability of optical label writing with this device has been demonstrated using PRBS data to modulate the EAM in the other transmitter arm. A modulation rate of 10 Gb/s was chosen, since this slower data rate would be more easily processed in a realistic optical router. A 2.0-V peak-to-peak drive signal was

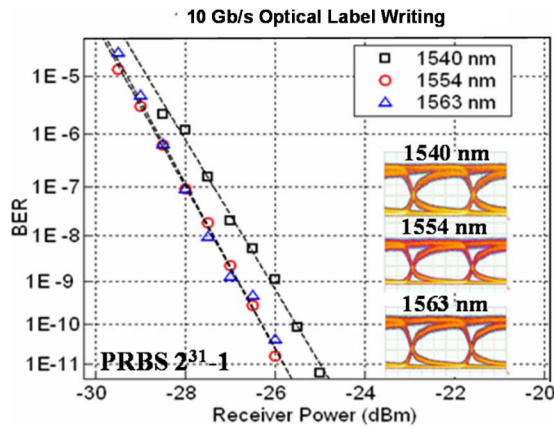


Fig. 21. BER measurements for external modulation of label-writing EAM at 10 Gb/s. Eye diagrams at each wavelength are shown.

applied by directly contacting the chip with a ground–signal–ground probe. Again, the dc bias for the EAM was adjusted to take advantage of the maximum modulation efficiency for each wavelength. Fig. 21 shows the BER for the 10 Gb/s modulation for varying output wavelengths. Less than 1 dB power penalty over the output tuning range was observed. The corresponding eyes diagrams demonstrate an output extinction ratio greater than 9 dB in all cases, and the output power was -6 to -6.5 dBm.

VII. CONCLUSION

This paper has presented a monolithic widely tunable wavelength converter based on a field-modulation technique. The device integrates a tunable SG-DBR laser, high saturation power SOAs, and high-speed EAM and PD, using a single regrowth fabrication process. The device geometry of each of the integrated components has been optimized to achieve efficient 40 Gb/s operation. The integrated receiver demonstrates >20 dB of gain and is capable of producing >30 mA of unsaturated photocurrent. The EAMs in this paper have demonstrated greater than 10 dB/V modulation efficiency over a wide optical bandwidth of 30 nm. Selective undercut etching and periodically loaded transmission lines have been used to double the characteristic impedance of the modulator for higher speed and increased voltage swing. Wavelength conversion has been demonstrated for 25 nm of input tuning and 22 nm output tuning, with 3 and 1 dB power penalty, respectively. The output extinction ratio of the converted signal was greater than 8 dB for all cases, with as high as -2 dB conversion efficiency. Conversion back to the same wavelength was demonstrated, as well as >40 dB input signal suppression at the output. This device also has been used for 10 Gb/s data transmission, which demonstrates potential for use in optical packet switched networks. Future work is focused on fast wavelength tuning to demonstrate packet routing as well as dynamic label encoding with simultaneous wavelength conversion. These experiments will confirm the viability of this wavelength converter in all-optical routing applications.

REFERENCES

- [1] S. Yoo, "Wavelength conversion technologies for WDM network applications," *J. Lightw. Technol.*, vol. 14, no. 6, pp. 955–966, Jun. 1996.
- [2] D. Blumenthal, B.-E. Olsson, G. Rossi, T. Dimmick, L. Rau, M. Masanovic, O. Lavrova, R. Doshi, O. Jerphagnon, J. Bowers, V. Kaman, L. Coldren, and J. Barton, "All-optical label swapping networks and technologies," *J. Lightw. Technol.*, vol. 18, no. 12, pp. 2058–2075, Dec. 2000.
- [3] M. Masanovic, V. Lal, J. Summers, J. Barton, E. Skogen, L. Rau, L. Coldren, and D. Blumenthal, "Widely tunable monolithically integrated all-optical wavelength converters in InP," *J. Lightw. Technol.*, vol. 23, no. 3, pp. 1350–1362, Mar. 2005.
- [4] V. Lal, M. Masanovic, J. Summers, L. Coldren, and D. Blumenthal, "Performance optimization of an InP-based widely tunable all-optical wavelength converter operating at 40 Gb/s," *IEEE Photon. Technol. Lett.*, vol. 18, no. 4, pp. 577–579, Feb. 2006.
- [5] P. Bernasconi, W. Yang, L. Zhang, N. Sauer, L. Buhl, I. Kang, S. Chandrasekhar, and D. Neilson, "40 Gbit/s RZ wavelength converter in a monolithically integrated chip with a tunable laser," *Electron. Lett.*, vol. 41, no. 12, pp. 701–702, 2005.
- [6] T. Yoshimatsu, S. Kodama, K. Yoshino, and H. Ito, "100-Gb/s error-free wavelength conversion with a monolithic optical gate integrating a photodiode and electroabsorption modulator," *IEEE Photon. Technol. Lett.*, vol. 17, no. 11, pp. 2367–2369, Nov. 2005.
- [7] M. Sysak, J. Raring, L. Johansson, H. Poulsen, J. Barton, D. Blumenthal, and L. Coldren, "Optical 2R and 3R signal regeneration in combination with dynamic wavelength switching using a monolithically integrated, widely tunable photocurrent driven wavelength converter," presented at the Eur. Conf. Opt. Commun. (ECOC), Cannes, France, Sep. 2006, Paper Th3.4.1.
- [8] M. M. Dummer, M. N. Sysak, A. Tauke-Pedretti, J. W. Raring, J. Klamkin, and L. A. Coldren, "Widely tunable separate absorption and modulation wavelength converter with integrated microwave termination," *J. Lightw. Technol.*, vol. 26, no. 8, pp. 938–944, Apr. 2008.
- [9] A. Tauke-Pedretti, M. Dummer, M. Sysak, J. Barton, J. Raring, J. Klamkin, and L. Coldren, "Monolithic 40 Gbps separate absorption and modulation Mach–Zehnder wavelength converter," in *Proc. Opt. Fiber Commun. Conf. (OFC) Postdeadline Papers*, Anaheim, CA, Mar. 2007, Paper PDP36.
- [10] M. Sysak, J. Raring, J. Barton, M. Dummer, D. Blumenthal, and L. Coldren, "A single regrowth integration platform for photonic circuits incorporating tunable SGDBR lasers and quantum-well EAMs," *IEEE Photon. Technol. Lett.*, vol. 18, no. 15, pp. 1630–1632, Aug. 2006.
- [11] Y. Muramoto, K. Kato, M. Mitsuhashi, O. Nakajima, Y. Matsuoka, N. Shimizu, and T. Ishibashi, "High-output-voltage, high speed, high efficiency uni-travelling-carrier waveguide photodiode," *Electron. Lett.*, vol. 34, no. 1, pp. 122–123, 1998.
- [12] N. Li, X. Li, S. Demiguel, X. Zheng, J. Campbell, D. Tulchinsky, K. Williams, T. Isshiki, G. Kinsey, and R. Sudharsanan, "High-saturation-current charge-compensated InGaAs-inp uni-traveling-carrier photodiode," *IEEE Photon. Technol. Lett.*, vol. 16, no. 3, pp. 864–866, Mar. 2004.
- [13] S. Demiguel, X. Li, N. Li, H. Chen, J. Campbell, J. Wei, and A. Anselm, "Analysis of partially depleted absorber waveguide photodiodes," *J. Lightw. Technol.*, vol. 23, no. 8, pp. 2505–2512, Aug. 2005.
- [14] V. Jayaraman, Z.-M. Chuang, and L. Coldren, "Theory, design, and performance of extended tuning range semiconductor lasers with sampled gratings," *IEEE J. Quantum Electron.*, vol. 29, no. 6, pp. 1824–1834, Jun. 1993.
- [15] Y.-J. Chiu, T.-H. Wu, W.-C. Cheng, F. Lin, and J. Bowers, "Enhanced performance in traveling-wave electroabsorption modulators based on undercut-etching the active-region," *IEEE Photon. Technol. Lett.*, vol. 17, no. 10, pp. 2065–2067, Oct. 2005.
- [16] T. Yamanaka, K. Tsuzuki, N. Kikuchi, E. Yamada, Y. Shibata, H. Fukano, H. Nakajima, Y. Akage, and H. Yasaka, "High-performance InP-based optical modulators," in *Proc. 2006 Nat. Fiber Opt. Eng. Conf. Opt. Fiber Commun. Conf.*, Anaheim, CA, 3 pp.
- [17] R. Lewen, S. Irmscher, U. Westergren, L. Thylen, and U. Eriksson, "Segmented transmission-line electroabsorption modulators," *J. Lightw. Technol.*, vol. 22, no. 1, pp. 172–179, Jan. 2004.
- [18] A. Tauke-Pedretti, M. Dummer, J. Barton, M. Sysak, J. Raring, and L. Coldren, "High saturation power and high gain integrated photoreceivers," *IEEE Photon. Technol. Lett.*, vol. 17, no. 10, pp. 2167–2169, Oct. 2005.



Matthew M. Dummer (S'06) received the B.S. degree in electrical engineering in 2002 from the University of Minnesota, Minneapolis, and the M.S. and Ph.D. degrees in electrical engineering in 2004 and 2008, respectively, from the University of California Santa Barbara (UCSB), Santa Barbara.

His thesis research focused on the development of high functionality photonic integrated circuits for wavelength conversion and optical routing. He also specialized in fabrication of high-power semiconductor optical amplifiers, and photodiodes, as well as traveling-wave circuit design for electroabsorption modulators. In 2008, he joined Vixar Inc. in Minneapolis, where he is currently working on the development of visible and long-wavelength vertical cavity surface emitting lasers (VCSELs).



Jonathan Klamkin (S'04) received the B.S. degree in electrical and computer engineering in 2002 from Cornell University, Ithaca, New York, the M.S. degree in electrical and computer engineering and the Ph.D. degree in materials from the University of California Santa Barbara (UCSB), Santa Barbara, in 2004 and 2008, respectively.

His thesis work focused on a novel coherent integrated receiver for highly linear microwave photonic links. In 2008, he joined the Electro-Optical Materials and Devices Group at MIT Lincoln Laboratory as a member of the Technical Staff. His research interests include the design, growth, fabrication, and characterization of widely-tunable semiconductor lasers, high power photodetectors, optical intensity and phase modulators, and semiconductor optical amplifiers for InP based photonic integrated circuits.



Anna Tauke-Pedretti (S'02–M'08) received the B.S. degree in physics and electrical engineering in 2001 from the University of Iowa, Iowa City, and the M.S. and Ph.D. degrees in electrical and computer engineering from the University of California Santa Barbara, Santa Barbara, in 2002 and 2007, respectively.

Her dissertation research involved the design, fabrication and testing of InP-based photonic integrated circuits for high-speed wavelength conversion. She has also developed monolithic high-speed transmitters and high-saturation power pre-amplified receivers. In 2008, she joined Sandia National Laboratories, Albuquerque, NM as a Senior Member of Technical Staff where she continues to work on the development of novel photonic integrated circuits.



Larry A. Coldren (S'67–M'72–SM'77–F'82) received the Ph.D. degree in electrical engineering from Stanford University, Stanford, CA in 1972.

He was engaged in research at Bell Laboratories for 13 years, where he was initially involved in the field of waveguided surface-acoustic wave signal processing devices and coupled-resonator filters and later developed tunable coupled-cavity lasers using novel reactive-ion etching (RIE) technology that he created for the new InP-based materials. In 1984, he joined the University of California Santa Barbara (UCSB), Santa Barbara, where he is currently the Fred Kavli Professor of optoelectronics and sensors and the Director of the Optoelectronics Technology Center, and was engaged in research on multiple-section tunable lasers, thus inventing, in 1988, the widely tunable multielement mirror concept. During the late 1980s, he also developed efficient vertical-cavity multiple-quantum-well modulators, which led to novel vertical cavity surface-emitting laser (VCSEL) designs that provided unparalleled levels of performance. In 1990, he cofounded Optical Concepts, later acquired as Gore Photonics, to develop novel VCSEL technology. In 1998, he cofounded Agility Communications to develop widely tunable integrated transmitters. His current research interests include developing new photonic integrated circuit (PIC) and VCSEL technology, including the underlying materials growth and fabrication techniques, creation of vertical and in-plane GaN-based emitters, efficient all-epitaxial InP-based VCSELs, and a variety of PICs incorporating numerous optical elements for widely tunable integrated transmitters, receivers, and wavelength converters. He has authored or coauthored more than 700 papers, five book chapters, one textbook, and is a holder of 36 patents.

Prof. Coldren has presented dozens of invited and plenary talks at major conferences. He is a Fellow of the Optical Society of America and the Institute of Electrical Engineers, and a member of the National Academy of Engineering. He was the recipient of the 2004 John Tyndall Award.